Microtesla MRI with a superconducting quantum interference device

Robert McDermott*†‡, SeungKyun Lee*†, Bennie ten Haken*†§, Andreas H. Trabesinger*¶‖, Alexander Pines*¶, and John Clarke*†

*Materials Sciences Division, Lawrence Berkeley National Laboratory, Berkeley, CA 94720; and Departments of †Physics and ¶Chemistry, University of California, Berkeley, CA 94720

Contributed by Alexander Pines, April 3, 2004

MRI scanners enable fast, noninvasive, and high-resolution imaging of organs and soft tissue. The images are reconstructed from NMR signals generated by nuclear spins that precess in a static magnetic field B_0 in the presence of magnetic field gradients. Most clinical MRI scanners operate at a magnetic field B_0 = 1.5 T, corresponding to a proton resonance frequency of 64 MHz. Because these systems rely on large superconducting magnets, they are costly and demanding of infrastructure. On the other hand, low-field imagers have the potential to be less expensive, less confining, and more mobile. The major obstacle is the intrinsically low sensitivity of the low-field NMR experiment. Here, we show that prepolarization of the nuclear spins and detection with a superconducting quantum interference device (SQUID) yield a signal that is independent of B_0, allowing acquisition of high-resolution MRIs in microtesla fields. Reduction of the strength of the measurement field eliminates inhomogeneous broadening of the NMR lines, resulting in enhanced signal-to-noise ratio and spatial resolution for a fixed strength of the magnetic field gradients used to encode the image. We present high-resolution images of phantoms and other samples and T_1-weighted contrast images acquired in highly inhomogeneous magnetic fields of 132 μT; here, T_1 is the spin-lattice relaxation time. These techniques could readily be adapted to existing multichannel SQUID systems used for magnetic source imaging of brain signals. Further potential applications include low-cost systems for tumor screening and imaging peripheral regions of the body.

The conventional MRI receiver coil operates on the principle of Faraday induction (1–4): the signal is therefore proportional to the product of sample magnetization and the frequency of nuclear spin precession. In the high-temperature limit, the thermal magnetization of the sample scales linearly with the magnetic field strength. Similarly, the nuclear precession frequency is proportional to the strength of the applied field. In the case of conventional detection, therefore, the NMR signal strength scales as B_0^2. The quadratic dependence of NMR signal on magnetic field has fuelled the drive to higher field strengths in MRI scanners for the last two decades, despite the disadvantages of converging T_1 times and increased energy deposition at higher frequencies.

At the same time, there has been continued interest in the development of MRI scanners that operate at low magnetic field strengths, of the order of the earth's field ($\approx$50 μT). Previous approaches to low-field MRI have relied heavily on techniques such as optical pumping (refs. 5 and 6, and ref. 7 and references therein) or prepolarization of the nuclear spins in a strong transient field (8–10) to generate enhanced, nonequilibrium nuclear magnetization and thereby boost the strength of the NMR signal. Tseng *et al.* (6) demonstrated MRI of hyperpolarized ^{3}He gas in a field of 2 mT. In the low-field imaging work of Macovski *et al.* (8, 9), the spins were prepolarized in a field of 0.3 T, while the NMR signals were detected in a much lower field of 30 mT. Using similar techniques, Stepišnik *et al.* (10) acquired MRIs in the magnetic field of the earth.

A complementary approach involves reduction of the noise of the NMR receiver (11), most notably by detecting the NMR signals with a dc superconducting quantum interference device (SQUID) (12). The dc SQUID consists of a superconducting loop interrupted at each of two points by a Josephson junction. When the SQUID is biased with a current I_b slightly above its critical current, the voltage across it is periodic in the flux applied to the loop, with a period of the flux quantum, $\Phi_0 = h/2e \approx 2 \times 10^{-15}$ T·m^2. A state-of-the-art low-transition temperature (low-T_c) SQUID can detect a magnetic flux change of $10^{-6}\,\Phi_0$ in a unit bandwidth. To increase its sensitivity to magnetic fields, the SQUID is often operated with a superconducting flux transformer, which consists of a pickup circuit (with inductance L_p) in series with an input coil (with inductance L_i) that is tightly coupled to the SQUID loop. Flux quantization implies that a flux applied to the pickup circuit generates a frequency-independent supercurrent in the transformer, which in turn couples flux to the SQUID. Thus, the untuned SQUID magnetometer detects broadband at arbitrarily low frequencies with no loss in sensitivity.

The unsurpassed sensitivity of the SQUID has been exploited as an alternative to conventional NMR detection since the 1980s (for a comprehensive review, see ref. 13). Although the majority of SQUID NMR studies were performed on solid samples at liquid helium temperatures, there have been several attempts at SQUID-detected MRI of room-temperature samples. For example, Schlenga *et al.* (14) used a high-T_c dc SQUID to image thermally polarized proton samples at room temperature in a field of 2 mT, while Seton *et al.* (15) used a low-T_c dc SQUID with a tuned input circuit to obtain MRIs of the human forearm in a field of 10 mT.

Recently, it was demonstrated (16, 17) that NMR detection with an untuned SQUID magnetometer in considerably lower fields (microtesla) can be used to enhance both spectral resolution and signal-to-noise ratio (SNR). For a sample magnetization that is fixed, for example by prepolarization, the frequency-independent response of the untuned SQUID implies that the integrated intensity of the NMR lines is independent of B_0. If the NMR linewidth is limited by magnetic field inhomogeneity, reduction of B_0 narrows the NMR lines, thereby improving spectral resolution. Because the detector is untuned, the amplitude of the NMR peak grows, leading to improved SNR.

Here we extend these ideas to MRI, where the reduction in B_0 enhances both SNR and spatial resolution for a fixed strength of the magnetic field gradients used to encode the image. In a one-dimensional MRI projection, the spatial resolution is

$$\Delta z = 2\pi\Delta f/\gamma G_z\,, \qquad [1]$$

Abbreviations: SNR, signal-to-noise ratio; SQUID, superconducting quantum interference device.

‡To whom correspondence should be sent at the present address: National Institute of Standards and Technology, Division 817, 325 Broadway, Boulder, CO 80305. E-mail: robertm@boulder.nist.gov.

§Present address: University of Twente, 7500 AE Enschede, The Netherlands.

‖Present address: Laboratory of Physical Chemistry, Eidgenössische Technische Hochschule, CH-8093 Zurich, Switzerland.

where Δf is the inhomogeneous width of the NMR line without applied gradients, γ is the magnetogyric ratio of the nucleus, and $G_z \equiv \partial B_z/\partial z$ is the magnetic field gradient applied to perform the frequency encoding. Although the conventional route to improved spatial resolution involves stronger magnetic field gradients G_z that disperse the NMR signal from the sample over a broader band, another approach is to reduce Δf. Because Δf scales with B_0 for fixed relative field homogeneity, decreasing B_0 improves the spatial resolution. In a SQUID MRI experiment performed in low field with linewidths approaching the lifetime limit, relatively high spatial resolution is achievable with modest magnetic field gradients, which disperse the NMR signal over only a narrow band. Consequently, the NMR transients are detected with high SNR, resulting in a relatively short MRI acquisition time.

Materials and Methods

Magnetic Field and Gradient Coils. The experiment is shown schematically in Fig. 1*a*. The SQUID MRI system incorporated three sets of coils to cancel the earth's field over the imaging region; a pair of coils to provide a weak measurement field B_0; four sets of gradient coils for image encoding and slice selection; a compact polarizing field coil; an excitation coil to provide audiofrequency pulses for nuclear spin manipulation; and a liquid helium dewar that housed the SQUID receiver. All support structures and coil forms were made from wood. Following the usual convention, we take the z axis to lie along the measurement field direction; the x axis is chosen to coincide with the vertical (detection) direction.

SQUID Receiver. Fig. 1*b* shows a block diagram of the detector circuitry. The low-T_c dc SQUID was based on niobium thin films and niobium–aluminum oxide–niobium tunnel barriers. The input circuit consisted of a niobium-wire pickup coil wound as a 1 + 2 + 1-turn, second-order axial gradiometer, with 150-mm baseline and 65-mm loop diameters, connected to a multiturn thin film niobium input coil integrated onto the SQUID chip. The effective sensing area of a single loop of the gradiometer was

$$A_{\text{eff}} = A_{\text{geo}} M/(L_{\text{i}} + L_{\text{p}}) \approx 9\ mm^2\,, \qquad [2]$$

where $L_{\text{i}} \approx 1.9\ \mu$H is the inductance of the input coil, $L_{\text{p}} \approx 1.7\ \mu$H is the inductance of the gradiometer pickup coils, $M \approx 11$ nH is the mutual inductance between the input coil and SQUID washer, and $A_{\text{geo}} \approx 3.2 \times 10^3$ mm^2 is the geometric area of a single gradiometer loop. The SQUID was current-biased in the voltage state and operated in a flux-locked loop (12) with flux modulation at 2 MHz. In this scheme, the signal from the SQUID is amplified, integrated, and fed back to the SQUID as a magnetic flux. The voltage across the feedback resistor is therefore proportional to the applied flux. In this way, the SQUID acts as a null detector of magnetic flux. When the SQUID was operated in a magnetically well shielded environment, the measured flux noise in the flux-locked loop was 7 $\mu\Phi_0 \cdot \text{Hz}^{-1/2}$, corresponding to a magnetic field noise of 1.6 $\text{fT} \cdot \text{Hz}^{-1/2}$ relative to the upper or lower loop of the gradiometer. The SQUID chip was enclosed in a superconducting niobium capsule to shield it from the large-amplitude transient magnetic fields used for nuclear spin manipulation.

Environmental Noise Reduction. Because of the exquisite intrinsic sensitivity of the SQUID, we took considerable care to ensure that the detector was not overwhelmed by external sources of magnetic field noise and interference. Except at 60 Hz and its harmonics, the magnetic field noise in our laboratory was of the order of 10 $\text{pT} \cdot \text{Hz}^{-1/2}$ at low frequencies (tens of Hz), decreasing to $\approx$1 $\text{pT} \cdot \text{Hz}^{-1/2}$ at a few kHz. Gradiometric configuration of the receiver coil reduces sensitivity to distant sources of noise and interference while maintaining high sensitivity to nearby signal sources. Our "as-made" second-order hardware gradiometer typically achieved a balance of better than 1:100 against uniform fields applied either in plane or out of plane. To reduce the environmental noise contribution further, we chose a measurement field to obtain an imaging band in a clean region of the environmental magnetic field spectrum; the broadband sensitivity of the untuned SQUID magnetometer offered consider-

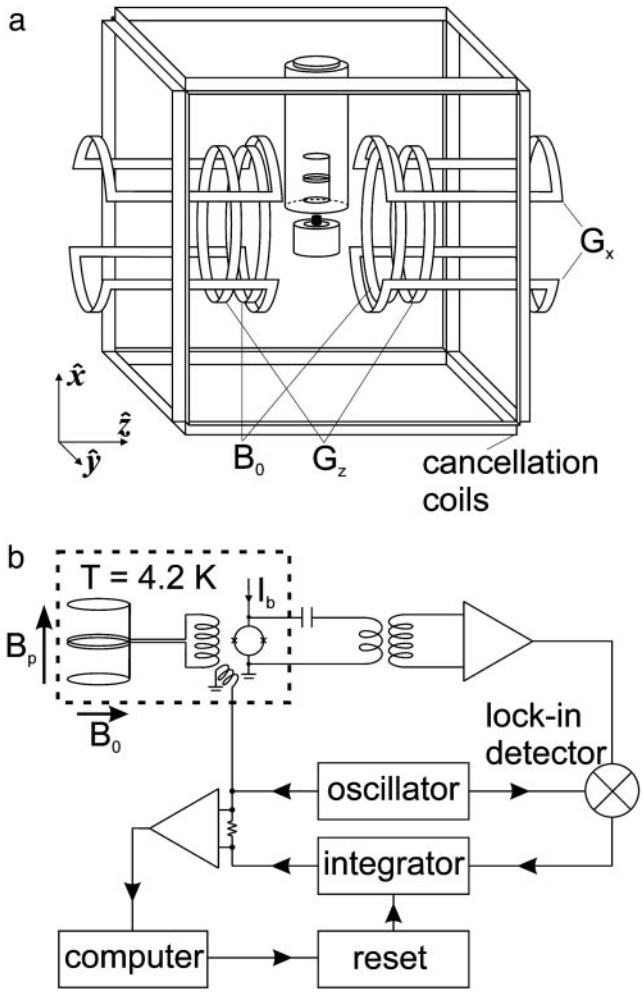

Fig. 1. Experimental apparatus. (*a*) Three orthogonal pairs of coils on a 1.8-m wooden cube cancelled the earth's field over the imaging region. A 1.2-m-diameter Helmholtz pair provided the measurement field B_0. Three sets of gradient coils provided frequency encoding: a 1.2-m-diameter Maxwell pair produced the longitudinal gradient $G_z \equiv \partial B_z/\partial z$, and two sets of saddle coils wound in the Golay (18) geometry on 1.2-m-diameter circular frames provided the transverse gradients $G_x \equiv \partial B_z/\partial x$ and $G_y \equiv \partial B_z/\partial y$. A set of biplanar gradient coils was used to produce large-amplitude slice selection gradient pulses G_x. For clarity, the coils for the G_y encoding gradient and for the slice selection gradient are not shown. The entire system was enclosed in a 3-mm-thick aluminum eddy current shield that eliminated radio-frequency interference and attenuated magnetic field fluctuations at the 5.6-kHz measurement frequency by an order of magnitude. (*b*) SQUID-based scanner for microtesla MRI. The thin-film dc SQUID was biased in the voltage state by a current I_b. The input coil, integrated on the SQUID chip, was connected to the superconducting pickup coil, which was wound from 75-μm niobium wire as a second-order, axial gradiometer. The gradiometer balance was better than 1:100 against uniform fields. The detector was immersed in liquid ^{4}He in a fiberglass dewar constructed in-house and designed to have low magnetic noise from the metallized thermal insulation (19, 20); the measured noise was <1 $\text{fT} \cdot \text{Hz}^{-1/2}$. The specimen to be imaged was placed beneath the dewar, $\approx$25 mm from the gradiometer sensing loop.

able freedom in the choice of measurement frequency. To avoid harmonics of the 60 Hz power line magnetic fields, we chose a center imaging frequency of 5.6 kHz, corresponding to a magnetic field of 132 μT. At this frequency we could implement passive shielding of the environmental magnetic field noise. We constructed an eddy-current shield from 3-mm-thick aluminum (5052 alloy) that surrounded the entire system. At 5.6 kHz, this thickness is roughly two skin depths, yielding a further order-of-magnitude attenuation of interfering magnetic fields. The combination of the gradiometer and the eddy-current shield effectively eliminated the environmental contribution to the magnetic field noise of the system. We ensured that the shield was radio-frequency-tight, to eliminate high-frequency interference that might reduce the flux-to-voltage transfer coefficient of the SQUID and thereby degrade system performance.

Low-Noise Cryostat. It was necessary to minimize the magnetic field noise contribution of the double-walled cryostat that was used to isolate the detector thermally from the room-temperature sample. To achieve a high filling factor in the MRI experiments, the sensing loop of the gradiometer was pressed flush against the bottom of the cryostat inner vessel. As a result, the SQUID was tightly coupled to any metallic components in the insulation jacket of the cryostat that generate Nyquist noise currents and, hence, magnetic field noise. Indeed, in the G-10 fiberglass cryostat originally used for these experiments, Nyquist currents in the aluminized mylar superinsulation or in the copper mesh of the thermal shield gave rise to a magnetic field noise of 10 fT·Hz$^{-1/2}$, exceeding by an order of magnitude the intrinsic noise of the SQUID gradiometer.

To reduce the magnetic field noise contribution of the superinsulation substantially, we constructed a G-10 fiberglass dewar based on the design of Seton *et al.* (19, 20). In this dewar, the normal metal thermal shield was replaced by a shield consisting of an array of 180 1-mm-diameter alumina rods attached to a thin G-10 fiberglass shell with epoxy. The thermal shield was anchored to the top of the inner vessel of the cryostat by 180 1-mm-diameter aluminum wires and was capped at the bottom with a thin alumina disk. Because the thermal shield had a high thermal conductivity, it was efficiently cooled by the helium gas that evaporated from the inner vessel. However, because the thermal shield was electrically insulating, it did not give rise to magnetic field noise. To minimize the noise contribution of the multilayer superinsulation, we replaced the conventional aluminized mylar with aluminized polyester fabric. In this case, the weave of the fabric ensures that the aluminum film is broken up into very small regions, thus preventing the flow of noise currents over large areas. The magnetic field noise generated by the metallization therefore falls away rapidly with distance from the superinsulation.

The inner vessel of the cryostat was 820 mm deep, and its inner diameter of 102 mm could easily accommodate the large-area pickup coils needed for SQUID MRI. The separation from the liquid helium space to the room temperature outside surface was $\approx$25 mm. The capacity of the cryostat was $\approx$6 liters, and the hold time was 40 h. The measured magnetic field noise of the cryostat was $<$1 fT·Hz$^{-1/2}$.

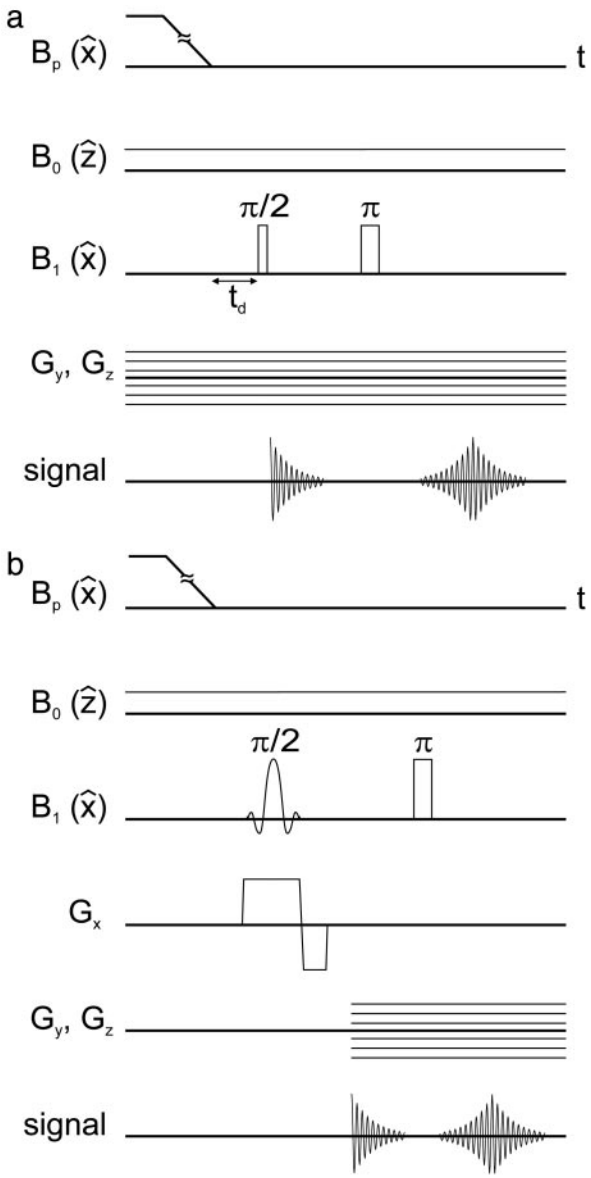

Fig. 2. (*a*) Pulse sequence for two-dimensional imaging with static gradients. The sample was first polarized in a field $B_p \approx 300$ mT along the detection direction $\hat{x}$ for a time $> T_1$. A measurement field $B_0 = 132$ μT was applied along $\hat{z}$. The polarizing field was turned off adiabatically in $\approx$20 ms, causing the nuclear spins to reorient along B_0. Subsequently, a resonant $\pi/2$ pulse tipped the spins into the x–y plane, where they precessed under the influence of B_0, G_y, and G_z. A resonant π pulse formed a spin echo that was detected by the SQUID gradiometer. The gradients G_y and G_z were stepped through successive values to rotate the direction of the resultant gradient. (*b*) Pulse sequence for slice selection MRI. Selection was achieved by means of a narrowband $\pi/2$ pulse of the form (sin x)/x, together with a strong gradient pulse $G_x \approx 400$ μT/m along the direction $\hat{x}$ normal to the plane of the slice.

MRI Pulse Sequences. Fig. 2*a* shows our MRI pulse sequence. The spins were prepolarized in a magnetic field $B_p \approx 300$ mT applied along the x direction for a time that was long compared to the spin-lattice relaxation time T_1. Upon adiabatic removal of the polarizing field, the nuclear spins reoriented to the direction of the measurement field $B_0 = 132$ μT, which was applied in a direction (z) orthogonal to the axis of the gradiometer. After a predetermined delay time t_d, a resonant $\pi/2$ pulse induced spin precession in the measurement field; the spin-echo (21) signal formed by a subsequent resonant π pulse was detected by the SQUID receiver. The flux-locked loop was enabled after application of the π pulse; the time preceding the formation of the echo allowed ample time for the loop to reset. A superconducting weak link incorporated in the gradiometer input circuit prevented large currents from being coupled to the input coil of the SQUID during spin manipulation.

To demonstrate the principle of microtesla field MRI, we used the conceptually simple method of projection reconstruction (1) to acquire two-dimensional images of MRI phantoms and other samples. In this technique, the direction of a static magnetic field gradient is stepped through successive angles to cover the

half-circle (in the y–z plane); at each gradient direction, a one-dimensional MRI projection is acquired. The one-dimensional projections are subsequently combined by using either filtered back projection (22) or interpolation to a Cartesian grid followed by a two-dimensional fast Fourier transform to obtain the full two-dimensional image.

In the MRI pulse sequence of Fig. 2*a*, the broadband $\pi/2$ pulse excites all nuclear spins in the sample. As a result, the MRI acquired with this sequence is a projection of the three-dimensional sample onto the y–z plane. To image a particular slice of the sample, one can apply a narrowband $\pi/2$ pulse designed to excite only the spins in the selected slice. In the sequence of Fig. 2*b*, a narrowband $\pi/2$ pulse with a sinc [$(\sin x)/x$] function envelope is applied in conjunction with a strong gradient pulse $G_x \approx 400\ \mu$T/m in the direction normal to the plane of the slice. The pulse excites only the spins in a slice of thickness $2\pi\delta f_1/\gamma G_x$, where δf_1 is the bandwidth of the $\pi/2$ pulse. After excitation, the gradient G_x is reversed to refocus the phase accumulated by the spins during slice selection. Subsequently, the encoding gradients G_y and G_z are switched on, and the remainder of the pulse sequence follows that of Fig. 2*a*.

Results

High-Resolution Imaging of MRI Phantoms. Fig. 3*a* shows the MRI acquired by using projection reconstruction from a phantom consisting of 13 columns of mineral oil. The strength of the applied magnetic field gradient was 200 μT/m; for each projection, 16 spin-echo signals were averaged together. The total averaging time was 7.5 min. Even the smallest column is well resolved, indicating a resolution of $\approx$1 mm.

T_1-Contrast Imaging. A commonly used technique in clinical MRI is T_1-contrast imaging (23): one either takes advantage of the different values of T_1 in different tissue types or introduces a paramagnetic contrast agent that shortens T_1 at sites at which it is selectively absorbed. Because nuclear relaxation processes are more strongly dependent on correlation times at low frequency than at high frequency, T_1 contrast is enhanced in low field (24, 25). Our experiment is ideally suited to probing T_1 in microtesla fields. To illustrate T_1-contrast imaging, we prepared a phantom containing four columns of water, two of which were doped with the paramagnetic contrast agent Gd-DOTA (Dotarem, Guerbet, Roissy, France). We imaged the sample repeatedly, varying the delay t_d between adiabatic removal of the polarizing field and application of the $\pi/2$ pulse. The results are displayed in Fig. 3*b*. The progressive changes in the relative intensities of the doped and undoped columns with t_d are a clear demonstration of T_1 contrast at 132 μT.

High-Resolution and Slice-Selected MRI of Peppers. As final examples, Fig. 4 shows two images of bell peppers acquired at 132 μT. In the first, a slice $\approx$10 mm thick was cut from the pepper and placed under the dewar. The two-dimensional image acquired by using the pulse sequence of Fig. 2*a* is shown in Fig. 4*a*. In the second case, an intact pepper was imaged, and the pulse sequence incorporated a narrowband $\pi/2$ pulse designed to excite only the spins in a 20-mm-thick slice $\approx$10 mm from the top of the pepper. The resulting image is shown in Fig. 4*b*. Both images demonstrate faithful reproductions of the pepper photographs, with a resolution of $\approx$1 mm.

Note on Concomitant Magnetic Field Gradients. As the measurement field B_0 is reduced to the point where it becomes comparable to the fields produced by the gradient coils, one encounters image artifacts due to unwanted concomitant gradient components that arise from the constraints div$\mathbf{B}$ = curl$\mathbf{B}$ = 0 on the total field $\mathbf{B}$ (26). For our experiments, however, these effects can be safely neglected, because the center imaging frequency is an order of magnitude larger than the imaging bandwidth. Indeed, a straightforward calculation shows that concomitant gradients produce a spatial misregistration of at most 0.5 mm at the sample edges.

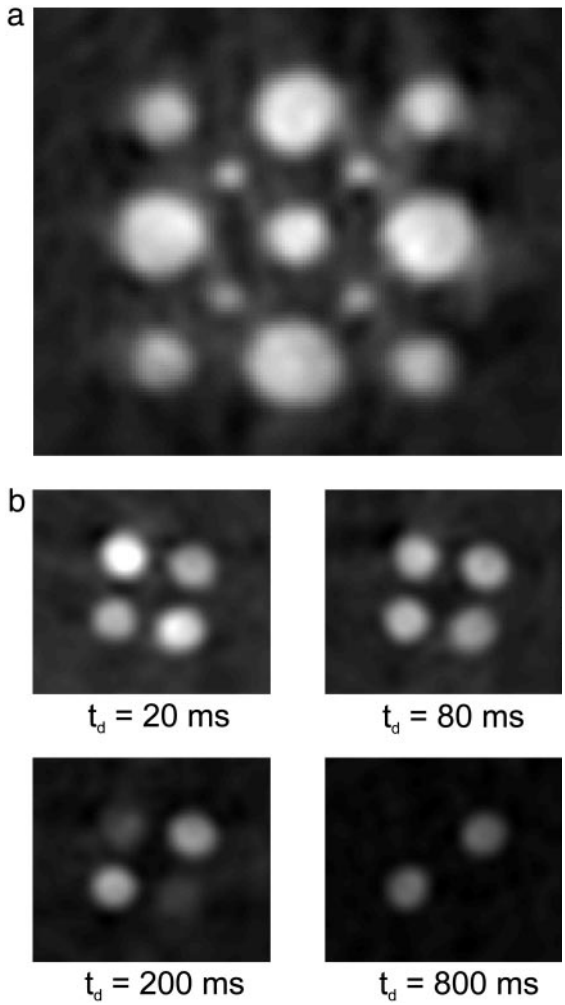

Fig. 3. Two-dimensional images of MRI phantoms. (*a*) Thirteen 40-mm long holes in a Teflon block were filled with mineral oil (proton density $\approx$100 M); the diameters were 3.2, 6.3, and 9.6 mm. The image was reconstructed from 48 one-dimensional projections acquired with B_0 = 132 μT and a gradient G = 200 μT/m. For each projection 16 spin-echo signals were averaged; the total acquisition time was 7.5 min. (*b*) T_1-contrast imaging at 132 μT. The phantom consisted of four columns of water, two of which (*Upper Left* and *Lower Right*) were doped with 1.0 mM Gd-DOTA to reduce T_1. The polarizing interval was 1 s; the delay time t_d (Fig. 2*a*) between adiabatic removal of the polarizing field and application of the $\pi/2$ excitation pulse was varied from 20 to 800 ms. For short delay times, the intensity of the doped columns was greater because these columns were more fully magnetized during polarization. For longer delay times, the relative intensity of the doped columns quickly diminished, as a result of T_1 relaxation.

Discussion

Although current imaging times are long by the standards of high-field MRI, reductions in system noise should speed acquisition substantially. In the typical high-field clinical scanner, the noise is set by inductively coupled losses in the human body. However, at the low frequencies characteristic of microtesla MRI, this noise source is negligible. For the experiments described above, the magnetic field noise of the SQUID MRI system was roughly 3 fT·Hz$^{1/2}$ and was dominated by Nyquist noise currents flowing in the copper wire of the polarizing coil. This source of noise could be substantially reduced by replacing the solid wire with a finely braided wire of the

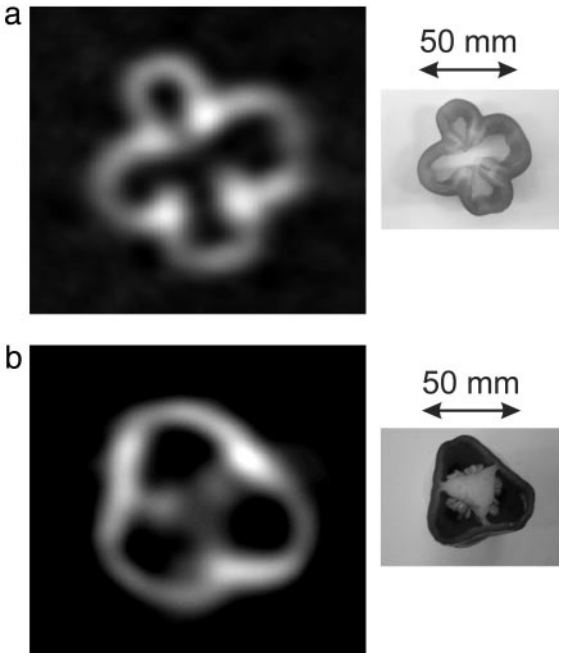

Fig. 4. MRI of peppers at 132 μT. (*a*) Two-dimensional image of sliced bell pepper ≈10 mm thick. The image was acquired with the pulse sequence of Fig. 2*a*, using 48 one-dimensional projections with $B_0 = 132$ μT and $G = 100$ μT/m. For each projection, eight spin-echo signals were averaged; the total acquisition time was 5 min. A photograph of the pepper slice is on the right. (*b*) Slice-selected image of whole pepper. The slice thickness was ≈20 mm. The image was acquired with the pulse sequence of Fig. 2*b*, using 48 one-dimensional projections with $B_0 = 132$ μT, $G = 100$ μT/m, and $G_x = 400$ μT/m. For each projection, four spin-echo signals were averaged; the total acquisition time was 3 min. A photograph of the pepper, cut *after* the MRI, is on the right.

same total cross section. Optimization of the SQUID could reduce its noise contribution from the current ≈1.6 fT·Hz$^{-1/2}$ by an order of magnitude. Thus, a system noise reduction of an order of magnitude is anticipated, resulting in single-shot data acquisition for each projection together with improved SNR. Multiple echo techniques should further improve the SNR (3, 4). Finally, to increase sensitivity to dipole sources, it would be advantageous to replace the single gradiometer with an array of smaller-area gradiometers, each coupled to its own SQUID. For a pickup loop of radius r, the signal flux coupled to the loop from a dipole scales approximately as r^{-1}, whereas the noise flux due to remote sources of interference scales as r^2. Thus, the use of a modest number of SQUID sensors could further improve the spatial resolution and acquisition efficiency dramatically. Multiple detectors have been used to advantage in high-field MRI (27).

Although low-field MRI will never supplant high-field scanners, there are certain applications in which its use may be exceedingly attractive. Microtesla MRI could be combined with existing commercial systems containing up to 300 SQUIDs that are used for magnetic source imaging (MSI), the measurement of weak neuromagnetic signals emanating from the brain (28, 29). Such systems are used clinically for presurgical screening of brain tumors and to locate sites responsible for focal epilepsy. However, it is essential to correlate the magnetic source data with anatomical structure; currently this requires a separate high-field MRI scan. The integration of MSI and MRI, for which the 300 sensors would greatly enhance the SNR, would create a new and versatile tool for clinical and research investigations of the brain. Furthermore, because the cost of a handful of SQUIDs and the associated cryogenic support, together with normal metal low-field magnets that do not require shimming to high homogeneity, is a small fraction of the cost of a high-field system, an inexpensive SQUID-based scanner could provide an alternative to conventional MRI in specific cases where considerations of cost or convenience take precedence. For example, microtesla MRI might be useful for the imaging of joints and extremities. Finally, SQUID-based MRI could be used for tumor screening, where the T_1-contrast capability would be an essential feature.

We thank Nathan Kelso, Darin Kinion, Michael Mück, and Whittier Myers for technical assistance, Hugh Seton for providing superinsulation and his plans for a low-noise dewar, and Song-I Han for suggestions on improving the manuscript. This work was supported by the Director, Office of Science, Office of Basic Energy Sciences, Division of Materials Sciences and Engineering of the U.S. Department of Energy. B.t.H. was supported by the Technology Foundation of the Netherlands Technology Foundation, the Applied Science Division of the Netherlands Organization for Scientific Research, and the Technology Program of the Ministry of Economic Affairs, and A.H.T. was supported by a postdoctoral fellowship from the Swiss National Science Foundation.

1. Lauterbur, P. C. (1973) *Nature* **242,** 190–191.
2. Mansfield, P. & Grannell, P. K. (1973) *J. Phys. C Solid State Phys.* **6,** L422–L426.
3. Callaghan, P. T. (1991) *Principles of Nuclear Magnetic Resonance Microscopy* (Clarendon, Oxford).
4. Haacke, E. M., Brown, R. W., Thompson, M. R. & Venkatesan, R. (1999) *Magnetic Resonance Imaging: Physical Principles and Sequence Design* (Wiley, New York).
5. Happer, W. (1972) *Rev. Mod. Phys.* **44,** 169–249.
6. Tseng, C. H., Wong, G. P., Pomeroy, V. R., Mair, R. W., Hinton, D. P., Hoffmann, D., Stoner, R. E., Hersman, F. W., Cory, D. G. & Walsworth, R. L. (1998) *Phys. Rev. Lett.* **81,** 3785–3788.
7. Goodson, B. M. (2002) *J. Mag. Res.* **155,** 157–216.
8. Macovski, A. & Conolly, S. (1993) *Magn. Reson. Med.* **30,** 221–230.
9. Shao, W., Wang, G., Fuzesy, R., Hughes, E. W., Chronik, B. A., Scott, G. C., Conolly, S. M. & Macovski, A. (2002) *Appl. Phys. Lett.* **80,** 2032–2034.
10. Stepišnik, J., Eržen, V. & Kos, M. (1990) *Magn. Reson. Med.* **15,** 386–391.
11. Darrasse, L. & Ginefri, J. C. (2003) *Biochimie* **85,** 915–937.
12. Clarke, J. (1996) in *SQUID Sensors: Fundamentals, Fabrication, and Applications*, ed. Weinstock, H. (Kluwer Academic, Dordrecht, The Netherlands), pp. 1–62.
13. Greenberg, Ya. S. (1998) *Rev. Mod. Phys.* **70,** 175–222.
14. Schlenga, K., McDermott, R., Clarke, J., de Souza, R. E., Wong-Foy, A. & Pines, A. (1999) *Appl. Phys. Lett.* **75,** 3695–3697.
15. Seton, H. C., Hutchison, J. M. S. & Bussell, D. M. (1997) *Meas. Sci. Technol.* **8,** 198–207.
16. McDermott, R., Trabesinger, A. H., Mück, M., Hahn, E. L., Pines, A. & Clarke, J. (2002) *Science* **295,** 2247–2249.
17. Trabesinger, A. H., McDermott, R., Lee, S.-K., Mück, M., Clarke, J. & Pines, A. (2004) *J. Phys. Chem. A* **108,** 957–963.
18. Bottomley, P. A. (1981) *J. Phys. E Sci. Instrum.* **14,** 1081–1087.
19. Seton, H. C., Bussell, D. M. & Hutchison, J. M. S. (2000) United Kingdom Patent GB2331798.
20. Seton, H. C., Bussell, D. M. & Hutchison, J. M. S. (2001) United Kingdom Patent GB2351549.
21. Hahn, E. L. (1950) *Phys. Rev.* **80,** 580–594.
22. Jain, A. K. (1989) *Fundamentals of Digital Image Processing* (Prentice–Hall, Englewood Cliffs, NJ).
23. Fischer, H. W., Rinck, P. A., Van Haverbeke, Y. & Muller R. N. (1990) *Magn. Reson. Med.* **16,** 317–334.
24. Carlson, J. W., Goldhaber, D. M., Brito, A. & Kaufman, L. (1992) *Radiology* **184,** 635–639.
25. Planinšič, G., Stepišnik, J. & Kos, M. (1994) *J. Magn. Reson. Ser. A* **110,** 170–174.
26. Norris, D. G. & Hutchison, J. M. (1990) *Magn. Reson. Imaging* **8,** 33–37.
27. Pruessmann, K. P., Weiger, M., Scheidegger, M. B. & Boesiger, P. (1999) *Magn. Reson. Med.* **42,** 952–962.
28. Vrba, J. (1996) in *SQUID Sensors: Fundamentals, Fabrication, and Applications*, ed. Weinstock, H. (Kluwer Academic, Dordrecht, The Netherlands), pp. 117–178.
29. Romani, G. L., Del Gratta, C. & Pizzella, V. (1996) in *SQUID Sensors: Fundamentals, Fabrication, and Applications*, ed. Weinstock, H. (Kluwer Academic, Dordrecht, The Netherlands), pp. 445–490.